Chemical Engineering Journal 545 (2026) 179443

Contents lists available at ScienceDirect

Chemical Engineering Journal

journal homepage: www.elsevier.com/locate/cej

High-performance hydrovoltaic smart window fabricated via laser-assisted printing for sustainable energy-saving buildings

Chao Chen [a,*], Jianhan Wang [a], Peijun Lin [a], Kai Shi [a], Long Zhang [a], Hongwen Zhang [b,*], Dong Wu [c], Yanlei Hu [c,*]

[a] Department of Materials Physics and New Energy Device, School of Materials Science and Engineering, Hefei University of Technology, Hefei, 230009, China
[b] Key Laboratory of Materials Physics, Anhui Key Laboratory of Nanomaterials and Nanotechnology, Institute of Solid State Physics, Hefei Institutes of Physical Science, Chinese Academy of Sciences, Hefei, 230031, China
[c] Department of Precision Machinery and Precision Instrumentation, University of Science and Technology of China, Hefei, 230026, China

ARTICLE INFO

Keywords:
Hydrovoltaic smart window
Thermoresponsive hydrogel
Superhydrophobic surface
Passive optical modulation
Sustainable building materials

ABSTRACT

Although hydrogel-based smart windows are promising energy-saving building components, they suffer from contamination-induced performance degradation and limited functionality. In this study, we report a zero-energy-consumption hydrovoltaic smart window (ZEC-HSW) that structurally combines optical regulation, self-cleaning, and droplet-induced energy harvesting. Owing to the reversible phase transition, the ZEC-HSW autonomously switches between transparent and opaque states, achieving a high visible transmittance modulation (ΔT_{vis} = 61.8%) and a large solar modulation ability (ΔT_{sol} = 46.3%). The bioinspired superhydrophobic surface (WCA ≈ 153°, WSA ≈ 3°) enables effective self-cleaning while being intrinsically coupled with raindrop-driven hydrovoltaic energy conversion, delivering an instantaneous voltage of ~30 V with stable output over 10,000 s. Thermal experiments and building simulations demonstrate a 7.5 °C reduction in indoor temperature, accompanied by average decreases of 34.66% in cooling energy consumption and 1756 kg in carbon emissions. This work establishes an integrated smart window strategy that unifies passive optical regulation, environmental self-maintenance, and droplet-enabled energy harvesting, offering a scalable strategy for sustainable buildings.

1. Introduction

The building sector accounts for approximately 40% of the total global energy consumption [1]. A significant portion of this energy is used by heating, ventilation, and air conditioning (HVAC) systems to maintain indoor thermal comfort. Windows account for up to 60% of building energy loss. However, they serve as an interface for energy exchange between indoor and outdoor environments and play a pivotal role in indoor temperature regulation [2]. Smart windows (SWs) offer a promising solution for reducing building energy consumption by dynamically regulating the transmission of solar radiation (including visible and near-infrared light) in response to external stimuli, such as temperature [3], electricity [4], mechanical stress [5], light [6], pH [7], and other factors [8,9]. However, existing SWs technologies largely address energy efficiency at the expense of system robustness, multi-functionality, or autonomous operation, leaving a critical gap in sustainable building integration.

Various stimulus-responsive materials have been explored for SWs applications. Among them, thermochromic materials, such as VO_2, have been widely studied owing to their passive regulation capability. VO_2 undergoes an insulator-to-metal phase transition at a specific critical temperature, switching from a transparent to a reflective state [10]. However, VO_2-based SWs are limited by a high transition temperature (T_{MIT} ≈ 68 °C) [11], generally low visible light transmittance (T_{lum} = 47.8%), and low solar modulation ability (ΔT_{sol} = 23.5%), which compromise visual comfort and energy-saving performance, severely hindering their practical application prospects [12]. Electrochromic SWs exhibit excellent solar modulation and fast response, enabling rapid switching between transparent and opaque states [13]. However, they require continuous external power supply, leading to additional energy consumption [14,15]. Mechanically responsive SWs modulate optical properties through deformation of surface morphology or internal structure (e.g., stretching or compression), which can induce light scattering to alter transmittance [16]. However, their optical modulation typically relies on large tensile strains, which may induce material fatigue and poses challenges for large-area applications.

* Corresponding authors.
E-mail addresses: chaoc11@ustc.edu.cn (C. Chen), hwzhang@issp.ac.cn (H. Zhang), huyl@ustc.edu.cn (Y. Hu).

https://doi.org/10.1016/j.cej.2026.179443
Received 19 April 2026; Received in revised form 7 June 2026; Accepted 12 July 2026
Available online 15 July 2026

Thermosensitive hydrogels, such as poly(N-isopropylacrylamide) (PNIPAM) [17], poly(N-vinylcaprolactam) [18], poly(N-isopropylmethacrylamide) [19], and hydroxypropyl cellulose [20], are highly promising candidate materials for SWs because they offer a combination of high visible light transmittance, good solar regulation capability, and passive operation [21]. These hydrogels are uniformly transparent below their lower critical solution temperature (LCST), allowing sunlight to penetrate indoors. Upon exceeding the LCST, they undergo a reversible phase transition from a transparent, hydrophilic state to an opaque, hydrophobic state, thereby reducing solar heat gain [22]. This transition mechanism is attributed to the reversible hydration and dehydration/collapse of polymer chains [23]. Consequently, hydrogel-based SWs can achieve fully autonomous solar regulation without the need for external energy input [24]. Recent studies have demonstrated that hydrogel SWs exhibit outstanding optical and energy-saving performance, highlighting their promising potential for next-generation energy-efficient buildings [25–28]. For instance, Long et al. reported a thermo-responsive hydrogel SW with a remarkable visible light transmittance (T_{vis} = 90%) and solar modulation ability (ΔT_{sol} = 68.1%); simulations showed that the SW reduced HVAC energy consumption by up to 44.6% compared to conventional glass [29]. Thus, thermoresponsive hydrogels represent not merely an alternative SW material, but a platform technology for sustainable building.

Despite their excellent optical modulation capability, the practical application of hydrogel SWs has been limited owing to environmental factors, such as dust accumulation and rain erosion. Surface contamination can significantly degrade transmittance and limit optical modulation capability [30], severely affecting long-term operational stability. This can be addressed using biomimetic superhydrophobic surfaces on SWs [31,32], which enable self-cleaning functionality. These surfaces exploit the low adhesion and rolling behavior of water droplets to remove contaminants and ensure long-term stability and optical clarity [33,34]. In particular, the self-cleaning process on such superhydrophobic surfaces offers potential for environmental energy harvesting. SWs with the dual functionality of passive energy saving and active energy generation can be achieved by converting the kinetic energy of raindrops into electrical energy and harvesting it during self-cleaning [35–40]. For example, Lee et al. designed a multifunctional SW integrating a triboelectric nanogenerator with a radiative cooler, capable of harvesting raindrop energy during rainfall and lowering indoor temperature via radiative cooling on sunny days [41]. However, such multifunctional smart windows typically rely on physically integrated but functionally decoupled components, where hydrovoltaic energy harvesting, optical regulation, and surface properties are achieved through separate layers, leading to increased system complexity and limited long-term robustness. In this regard, we tend to propose a zero-energy-consumption hydrovoltaic SW (ZEC-HSW) based on the synergistic integration of a thermoresponsive hydrogel, a transparent conductive layer, and a laser-assisted microstructured surface. The novelty of this design lies in the use of the microstructured surface as a multifunctional interface that couples long-term optical stability with droplet-induced electricity generation. The thermoresponsive hydrogel enables reversible optical modulation in response to temperature changes. More importantly, the laser-assisted microstructured surface provides superhydrophobic self-cleaning behavior, which helps remove water droplets and surface contaminants and thereby supports the long-term outdoor optical transparency of the hydrogel smart window. Meanwhile, the same microstructured surface facilitates droplet contact/separation and rapid droplet shedding, contributing to stable droplet-induced electricity generation. This microstructure-enabled synergistic design distinguishes the present ZEC-HSW from conventional hydrogel smart windows and droplet-based energy harvesters.

In this study, we fabricate a ZEC-HSW that unifies optical regulation, superhydrophobic self-maintenance, and droplet-induced energy harvesting within a single material–device architecture to address the functional decoupling and long-term instability of existing hydrogel SWs. The device features a sandwich structure combining a femtosecond-laser-printed transparent, superhydrophobic droplet energy generator (DEG) with a PNIPAM/hydroxypropyl methylcellulose (HPMC) hydrogel layer. Leveraging the reversible phase transition of the hydrogel, the SW can thermally switch between transparent and opaque states, achieving excellent visible light transmittance and solar modulation ability. Simultaneously, the biomimetic superhydrophobic surface confers superior self-cleaning capability, effectively repelling various liquids and removing particulate contaminants. Finally, temperature regulation and droplet-based power generation capabilities of the SW are demonstrated. This study not only provides a practical solution to the contamination issue affecting hydrogel SWs but also offers a new strategy for developing multifunctional SWs.

2. Results and discussion

2.1. Laser-assisted facile fabrication of dual-mode ZEC-HSW

We propose a ZEC-HSW to overcome the limitations inherent to traditional hydrogel SWs. Under sunny conditions, the ZEC-HSW dynamically modulates solar transmittance to regulate indoor heat; under rainy conditions, it stays transparent while harvesting droplet energy for self-cleaning and power generation. This optical switching relies on the hydrogel's reversible phase transition. Below the LCST, the PNIPAM/ hydroxypropyl methylcellulose (HPMC) hydrogel remains highly hydrated and optically homogeneous, allowing efficient light transmission. Above the LCST, PNIPAM chains undergo dehydration and local aggregation, generating refractive-index heterogeneity that strongly scatters visible light. Meanwhile, the HPMC cellulose network serves as a supporting framework that restricts large-scale hydrogel shrinkage. Therefore, the transparent-to-opaque transition originates mainly from internal micro/nanoscale phase separation rather than obvious macroscopic volume contraction. Furthermore, the droplet energy generator (DEG) converts the mechanical energy of raindrops into electrical output. In this process, a capacitor (C_1) forms at the interface between the shape memory polymer (SMP) and the indium tin oxide (ITO) layer. Meanwhile, the solid–liquid interface between the raindrop and the SMP surface creates a second capacitor (C_2). Additionally, when the droplet comes contact with the copper electrode, a third capacitor (C_3) is established at the droplet–copper interface. At this stage, charge transfer occurs along the closed loop, thereby generating a transient voltage [42–44].

The proposed ZEC-HSW was fabricated via eight key steps as follows. (i) A soft transfer template featuring a closely packed hexagonal array was fabricated via direct writing on a polytetrafluoroethylene (PTFE) film (thickness ~ 200 μm) using a regeneratively amplified Ti:sapphire femtosecond laser system (Fig. 1A-i). The following laser parameters were used: 800 mW power, 10 kHz repetition rate, 8 scans, and 150 mm s^{-1} scanning speed. The side length of the laser-scanned hexagonal pattern was 500 μm. The exceptional peak power of the femtosecond laser enables precise ablation, ensuring high fidelity of the micro-cavities [45,46]. This laser-printed micro-cavity architecture provides a deterministic structural template for subsequent replication, ensuring uniform cavity geometry that is essential for stable superhydrophobicity and interfacial charge generation. (ii) Subsequently, a mixture of epoxy prepolymer and curing agent was cast onto the template and placed under vacuum for 1 h. This process ensures high-fidelity replication of the micro-cavity architecture, which is critical for subsequent superhydrophobic stabilization and structure preservation. (iii) An ITO glass slide, pre-attached with copper tape electrodes at the corners, was then placed over the partially cured SMP layer under a pressure of 20 N. The transparent conductive layer acts as the electrical backbone for droplet-induced hydrovoltaic energy harvesting and enables efficient charge collection without compromising optical transparency. (iv) After thermal curing at 65 °C for 4 h, the demolded micropillar array was firmly bonded to the ITO glass, resulting in a DEG substrate with the SMP

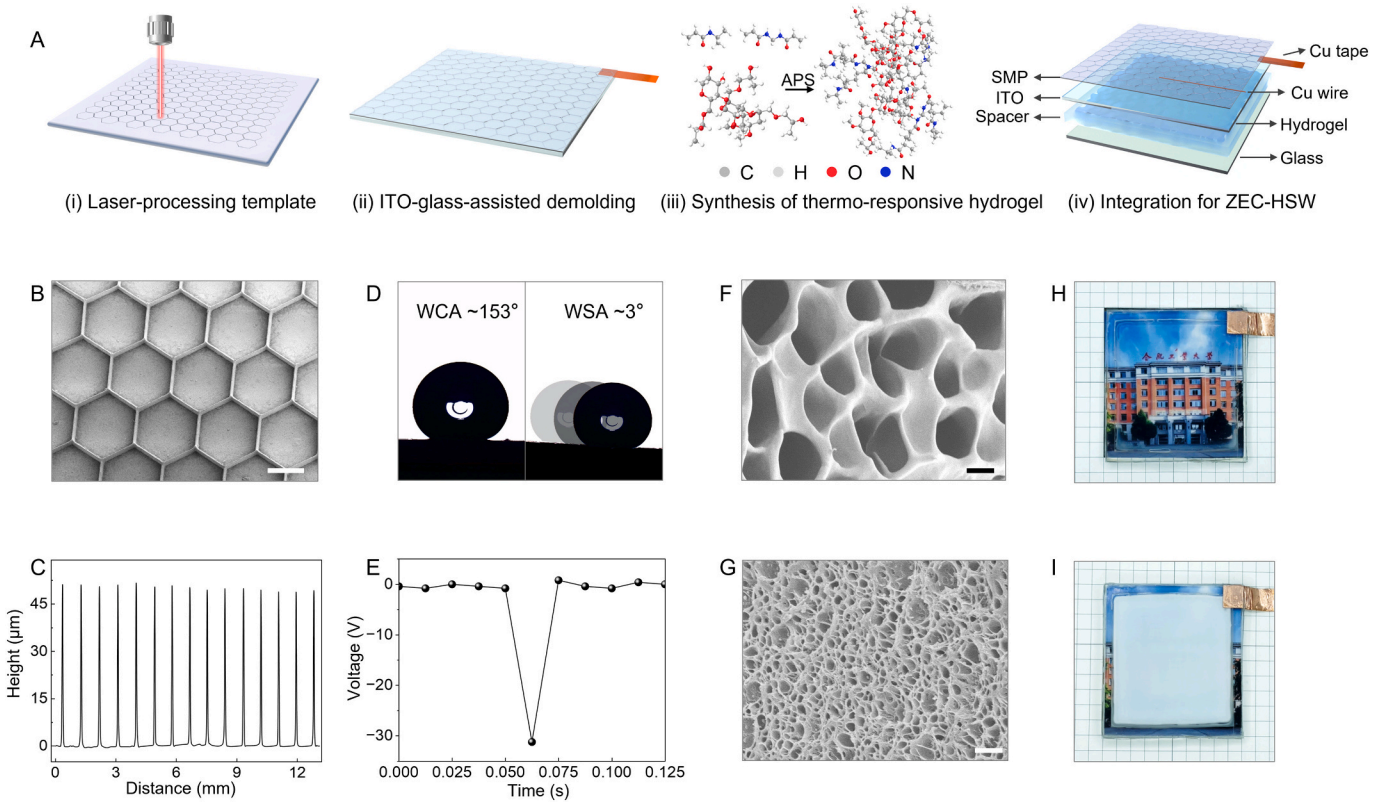

Fig. 1. Facile fabrication and structural characterization of the ZEC-HSW. (A) Schematic of the fabrication process, including (i) femtosecond laser patterning of a PTFE template, (ii) SMP replication and lamination with ITO glass, (iii) hydrogel precursor injection, and (iv) final device assembly with electrodes. (B) SEM image of the uniform hexagonal honeycomb microstructure (scale bar: 500 μm). (C) 3D confocal microscopy image showing the replicated micropillar array with a height of ~50 μm and spacing of ~900 μm. (D) Water contact angle (WCA ≈ 153°) and sliding angle (WSA ≈ 3°) measurements demonstrating superhydrophobicity. (E) Typical voltage output (~30 V within 12.5 ms) generated by a droplet impacting the transparent DEG substrate. (F, G) SEM images of freeze-dried PNIPAM hydrogel samples corresponding to the hydrated transparent state and dehydrated opaque state, respectively (scale bars: 1 μm and 500 nm). (H, I) Digital photographs showing the reversible optical switching between high-transparency and opaque states.

micro-array (Fig. 1A-ii). (v) To achieve effective liquid repellency, a superhydrophobic coating containing hydrophobic silica nanoparticles was spin-coated onto the SMP micro-array, followed by heat treatment. This superhydrophobic modification not only endows the surface with self-cleaning capability, but also reduces the interfacial adhesion between the solid phase and the liquid drop, while shortening the droplet's dwelt time, which is a prerequisite for stable interfacial charge separation and repeatable hydrovoltaic output. (vi) A silicone gel square frame (thickness 1 mm) fabricated via femtosecond laser cutting was used to assemble a sandwich structure by bonding the ITO glass to a plain glass slide. (vii) A PNIPAM hydrogel precursor was prepared using N-isopropylacrylamide (NIPAM), *N,N′*-methylenebisacrylamide (MBA), HPMC, ammonium persulfate (APS), and $NaHSO_3$ (Fig. 1A-iii) and injected into the cavity enclosed by the silicone frame. By confining the thermoresponsive hydrogel within the microcavity array, its intrinsic phase transition is translated into a geometry-regulated optical response, enabling pronounced and reversible light modulation under fully passive thermal stimuli. (viii) Finally, connect the copper wire electrode to the bottom of the SMP surface to complete the device assembly (Fig. 1A-iv).

Scanning electron microscopy (SEM) images revealed a highly uniform and continuous hexagonal honeycomb array (Fig. 1B), demonstrating the high fidelity of the structure transfer process. The dimensions of the micro-array were further quantified via laser scanning confocal microscopy; the results indicated micropillar heights of approximately 50 μm and edge-to-edge spacings of approximately 900 μm (Fig. 1C; Fig. S1). This highly uniform and well-defined honeycomb array serves a dual purpose: (i) it provides a robust scaffold for the superhydrophobic coating, preventing the detachment of silica nanoparticles (Fig. S2) under abrasion; (ii) The SMP micro-array provides a roughened interfacial architecture with enlarged geometric surface area and increased three-phase contact-line length during transient droplet impact, thereby enhancing interfacial charge generation and charge transfer. Thus, the SMP micro-array exhibits excellent water-repellent properties owing to the synergistic effects of the micropillar array and hydrophobic coating. As shown in Fig. 1D, the substrate exhibited a water contact angle (WCA) of 153° and a water sliding angle (WSA) of 3°, confirming its superhydrophobicity. Based on the hydrophobic microstructure and underlying electrode configuration, we demonstrate its function as a DEG. Fig. 1E shows a typical voltage output signal, indicating an instantaneous voltage of approximately 30 V within a very short time (12.5 ms) after droplet impact. This result confirms the energy conversion capability of the substrate, showcasing its potential for ambient energy harvesting. The integration of the PNIPAM hydrogel is key to the optical switching of the ZEC-HSW. The microstructural change associated with the optical switching was qualitatively examined using SEM images of freeze-dried hydrogel samples prepared at different thermal states. Although freeze-drying may not fully reproduce the exact in situ hydrated morphology, it is a widely used method for observing the internal network of thermoresponsive hydrogels. Therefore, the SEM results were used as qualitative morphological evidence. The SEM images of the hydrated state at low temperature (Fig. 1F, G) revealed a uniform porous structure with pore sizes ranging between 4 and 8 μm (Fig. S3). In contrast, in the high-temperature dehydration state, the porous network was replaced by a non-uniform structure comprising polymer aggregation regions and micropores. The sizes of these features

were comparable to the wavelength of visible light, resulting in strong light scattering. Fig. 1H, I, demonstrates the optical switching effect: a highly transparent state at low temperature, wherein the underlying pattern is clearly visible, and an opaque, milky-white state at high temperature that effectively blocks the view (Supporting information, Movie S1). In summary, by leveraging the synergy between the superhydrophobic SMP substrate and the thermoresponsive hydrogel layer, we have successfully fabricated a ZEC-HSW that integrates surface superhydrophobicity, hydrovoltaic power generation, and autonomous solar regulation into a single device. The design of ZEC-HSW is based on a synergistic structure–function relationship rather than a simple stacking of independent components. The thermoresponsive hydrogel is responsible for adaptive optical modulation, whereas the laser-assisted microstructured surface provides an additional functional interface for outdoor operation. This microstructured interface enables superhydrophobic self-cleaning, which helps maintain optical transparency by reducing water retention and contaminant adhesion. At the same time, the microstructure also benefits droplet-induced electricity generation by promoting repeated liquid–solid contact/separation and efficient droplet departure. Therefore, the microstructured surface serves as a bridge between the smart-window function and the energy-harvesting function.

2.2. Optical switching performance of the ZEC-HSW

The ZEC-HSW's thermosensitive hydrogel layer passively modulates sunlight. Upon solar irradiation, absorbed energy is converted into heat and transferred to the hydrogel, raising its temperature above the LCST. Consequently, polymer chains contract, and the hydrogel transitions from a transparent to an opaque state. Cooling below the LCST reverses this process, restoring the transparent state (Fig. 2A). The phase transition dynamics and underlying mechanism were investigated via variable-temperature fourier transform infrared spectroscopy (VT-FTIR) and differential scanning calorimetry (DSC). VT-FTIR (20–40 °C) shows a broad centered at ~3400 cm^{-1} band from O–H/N–H stretching; its peak shift with temperature reveals hydrogen-bonding changes during the phase transition (Fig. 2B). Although this band persisted across the entire temperature range, its peak position shifted with an increase in temperature, reflecting changes in the hydrogen-bonding environment during the PNIPAM phase transition. At low temperature, strong

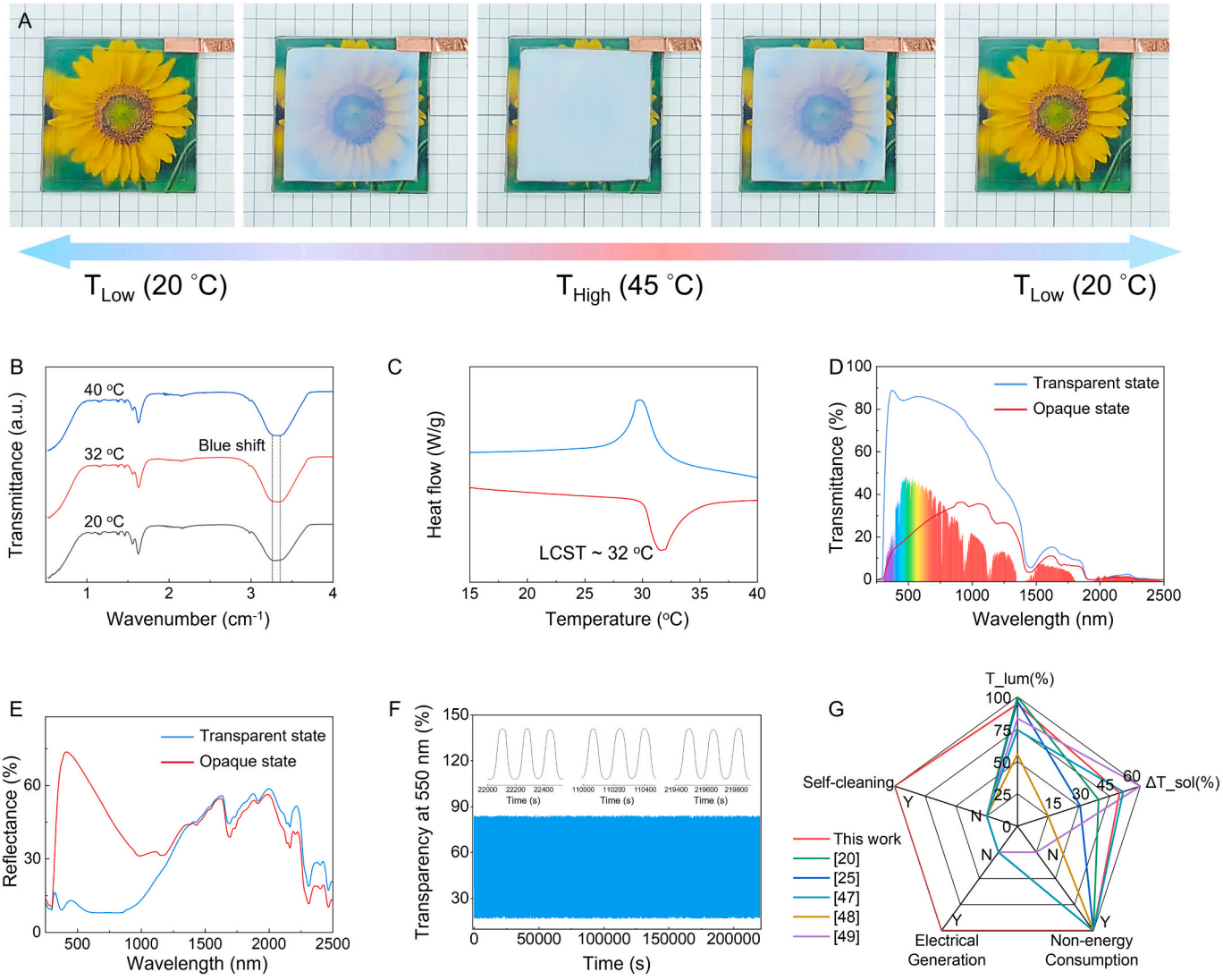

Fig. 2. Optical switching performance of the ZEC-HSW. (A) Schematic of the reversible transparent-to-opaque transition triggered by temperature change. (B) VT-FTIR spectra showing the evolution of hydrogen bonding during the phase transition. (C) DSC curve indicating a LCST of ~32 °C. (D) UV–Vis–NIR transmittance spectra of the ZEC-HSW in both transparent and opaque states, spanning 300–2500 nm. (E) Corresponding reflectance (300–2500 nm). (F) The durability test results of transmittance cycling after 1000 heating/cooling cycles at 550 nm. (G) Comprehensive performance comparison between the current ZEC-HSW and other reported smart windows.

hydrogen bonds (e.g., N–H···O=C and O–H···O) form among the PNIPAM amide groups, HPMC hydroxyl groups, and water molecules, resulting in a highly hydrated network. As the temperature approaches the LCST, dehydration weakens these interactions, evidenced by a blue shift of the peak from 3296.1 to 3336.7 cm^{-1}, followed by a further shift to 3352.6 cm^{-1} at higher temperature, corresponding to the hydrophobic collapse of PNIPAM chains. DSC measurements further confirmed the thermal transition behavior of the hybrid hydrogel (Fig. 2C), revealing an LCST of approximately 32 °C under heating and cooling rates of 10 °C/min. The solar modulation capability of the ZEC-HSW was examined by studying its optical performance via ultraviolet–visible–near-infrared (UV–Vis-NIR) spectroscopy. As shown in Fig. 2D, the optical transmittance of the ZEC-HSW spanned the 300–2500 nm range, making it suitable for both optical and thermal management applications. In the transparent state at low temperature, the transmittance peak reached 87% at 550 nm, demonstrating the exceptional optical clarity of the ZEC-HSW. Conversely, in the opaque state at high temperature, T_{550} decreased to 18%. Additionally, we measured the reflectance (R) of the ZEC-HSW in the 300–2500 nm range and the absorptivity (A) in the 2.5–25 μm range (Fig. 2E; Fig. S4). In the opaque state, the ZEC-HSW exhibited strong reflectance within the solar spectrum and high absorbance in the mid-infrared region. The transmission performance of the ZEC-HSW in both states for visible light ($T_{380–780}$), infrared ($T_{780–2500}$), and the full solar spectrum ($T_{380–2500}$) was quantified using the following empirical formulas [29]:

$$T_{vis/IR/sol} = \frac{\int \varphi_{vis/IR/sol}(\lambda) T(\lambda) d\lambda}{\int \varphi_{vis/IR/sol}(\lambda) d\lambda}$$

and

$$\Delta T_{vis/IR/sol} = T_{vis/IR/sol}\ (\text{transparent status}) - T_{vis/IR/sol}\ (\text{opaque status})$$

where φ_{vis} represents the photopic efficiency function of the human eye, and $\varphi_{IR/solar}$ represents the AM1.5 solar irradiance spectrum. In the transparent state, $T_{380–780}$, $T_{780–2500}$, and $T_{380–2500}$ reached 85.4%, 57.2%, and 72.2%, respectively. Upon switching to the opaque state, the respective values decreased to 23.6%, 28.6%, and 25.9%. Consequently, the calculated modulation abilities were ΔT_{vis} = 61.8% and ΔT_{sol} = 46.3%. The optical spectra of devices without the laser-induced microstructure or without the superhydrophobic coating are provided in Fig. S11 to clarify the contribution of different functional layers. In particular, the ZEC-HSW exhibited preliminary stability under cyclic temperature changes, with the transmittance at 550 nm remaining

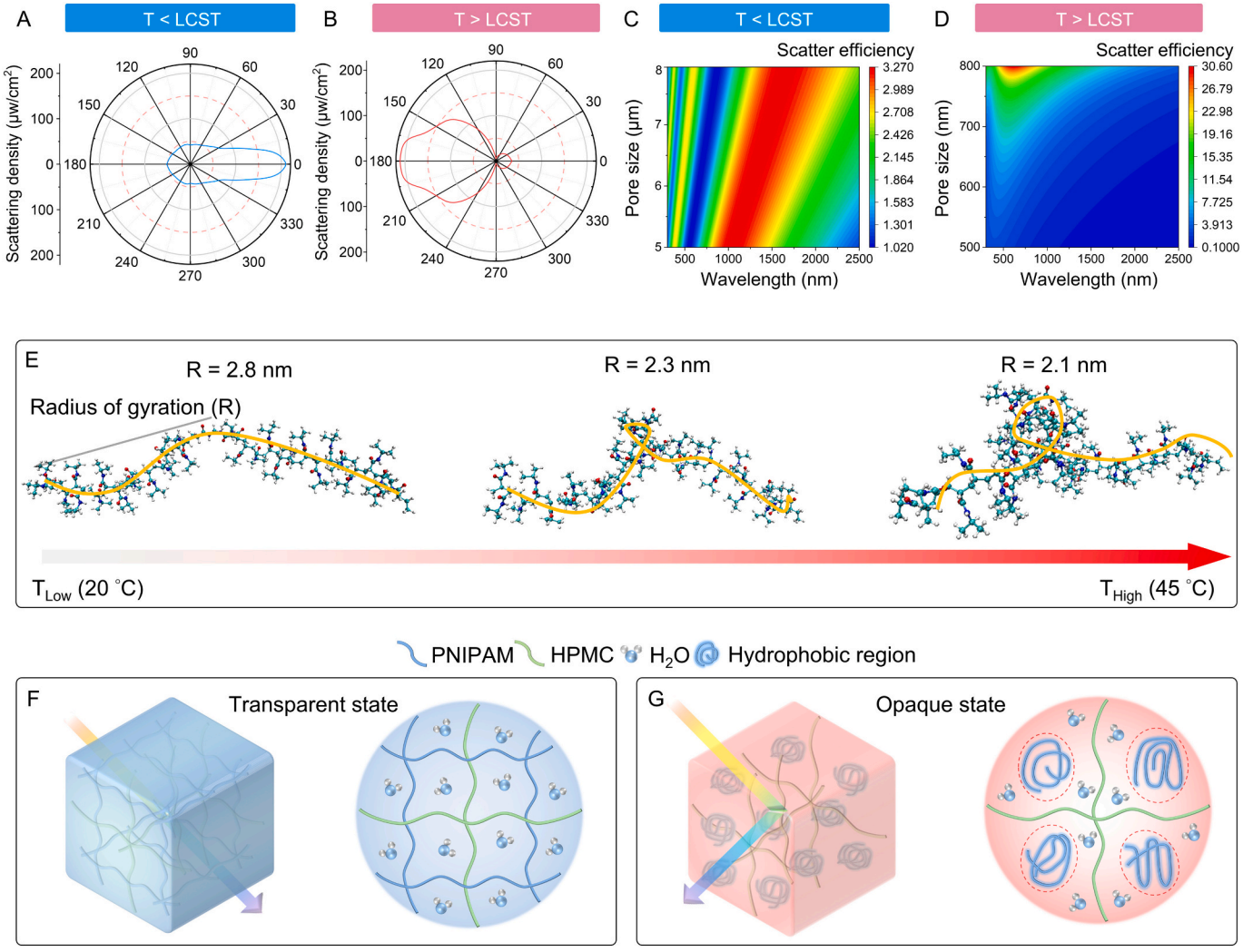

Fig. 3. Optical switching mechanism of the PNIPAM hydrogel. (A, B) Laser scattering patterns at 550 nm for the hydrogel below (20 °C) and above (40 °C) the LCST, respectively, indicating a scattering-dominated opacity mechanism. (C, D) FDTD-simulated scattering efficiency spectra for the hydrogel in the transparent (water-filled pores) and opaque (air-filled pores) states. (E) Molecular dynamics simulation snapshots illustrating the conformation change of PNIPAM chains from hydrated and extended (below LCST) to dehydrated and collapsed (above LCST). (F, G) Proposed unified mechanism: the hydrogel remains optically homogeneous and transparent below the LCST, while dehydration-induced microphase separation generates Mie-scattering centers above the LCST, leading to macroscopic opacity.

stable after 1000 heating/cooling cycles (Fig. 2F). These values place the ZEC-HSW among the competitive performance passive hydrogel-based SWs reported to date, while maintaining zero-energy operation. A comprehensive performance comparison is presented in Fig. 2G. Compared to previously reported SWs [20,25,47–49], our ZEC-HSW exhibits a well-balanced overall performance in terms of visible light transmittance ($T_{vis} = 85.4\%$), solar modulation ability ($\Delta T_{sol} = 46.3\%$), zero-energy operation, self-cleaning capability, and power generation functionality.

2.3. Optical switching mechanism of ZEC-HSW

The light-switching behavior of the PNIPAM hydrogel was directly visualized using a 550 nm laser. At 20 °C, the incident light propagated predominantly in the forward direction with negligible scattering, indicating a transparent state. In contrast, at 40 °C, the transmitted light was strongly attenuated and scattered in multiple directions (Fig. 3A, B). These results indicate that the optical switching is governed by a scattering-dominated mechanism. The underlying physical mechanism of the observed scattering behavior was investigated via a finite-difference time-domain (FDTD) simulation. The hydrogel was modeled as a matrix containing water-filled pores (transparent state) and air-filled pores (opaque state) (Fig. S5). The pore sizes used in the simulation were extracted from the SEM images of the hydrogel microstructure (Fig. 1F, G). Weak wavelength-dependent scattering with interference fringes, originating from coherent reflections within micrometer-sized water-filled pores, was observed in the transparent state, consistent with low optical loss (Fig. 3C, D). Upon phase transition, the scattering efficiency increased sharply across the 300–1000 nm range, reaching a maximum value of ~30.6. This increase is attributed to the formation of heterogeneous polymer-rich domains and micropores with characteristic dimensions comparable to visible light wavelengths, which act as effective Mie scattering centers, rendering the hydrogel opaque [50,51]. Collectively, these results demonstrate that the optical switching of the ZEC-HSW is not a simple phase-opacity transition, but a scattering-dominated macroscopic light modulation. Molecular dynamics simulations further revealed the microscopic mechanism underlying the phase transition (Fig. 3E). At low temperature, PNIPAM chains adopt hydrated, extended conformations stabilized by hydrogen bonding with surrounding water molecules. These hydrogen bonds progressively weaken with an increase in temperature, leading to dehydration and entropy-driven hydrophobic collapse of the polymer chains. This process is quantitatively reflected by a reduction in the radius of gyration from 2.2 to 1.5 nm and a contraction of the end-to-end distance from 2.8 to 2.1 nm (Fig. S6). The dehydration process triggers the aggregation of hydrophobic isopropyl groups via hydrophobic interactions. Although this reduces the entropy of the polymer chains, it releases bound water molecules, leading to a significant increase in the entropy of the water that drives the phase transition. Thus, the redistribution of hydrogen bonds facilitates dehydration and chain collapse (Fig. S7). We propose a unified optical switching mechanism based on the results of experiments and multiscale simulations (Fig. 3F, G). Below the LCST, the hydrogel remains optically homogeneous, resulting in low scattering loss and high transmittance. Above the LCST, dehydration-induced chain collapse generates a multiphase microstructure that strongly scatters incident light via Mie resonance, causing a macroscopic transition of the ZEC-HSW from the transparent to opaque state, effectively blocking solar radiation. Notably, the micro/nanoscale structural reorganization of the PNIPAM/HPMC hydrogel does not necessarily result in visible macroscopic shrinkage. Above the LCST, the Hofmeister effect modulates the hydration state of PNIPAM chains by weakening polymer–water interactions, thereby promoting local dehydration and hydrophobic collapse of PNIPAM into polymer-rich aggregates with characteristic sizes of approximately 400–800 nm [52]. These polymer-rich domains generate refractive-index heterogeneity and act as efficient light-scattering centers. However, the water released from PNIPAM dehydration is not expelled from the bulk hydrogel; instead, it is redistributed and retained within the hydrophilic HPMC network and its nanoporous/free-volume regions. Moreover, the HPMC cellulose-based network serves as a relatively rigid mechanical scaffold [53], which confines the thermally induced PNIPAM reorganization to localized micro/nanoscale domains and prevents it from propagating into macroscopic volume contraction. Therefore, the transparent-to-opaque transition mainly arises from local phase separation and internal water redistribution within the constrained PNIPAM/HPMC network, rather than from obvious bulk shrinkage.

2.4. Superhydrophobicity and self-cleaning functionality of the ZEC-HSW

The micro/nanostructured SMP surface and superhydrophobic coating give the ZEC-HSW robust self-cleaning, ensuring long-term optical clarity. As shown in Fig. 4A, it repels water, ethylene glycol, milk, coffee, and glycerol. Quantitative wetting characterization revealed a high WCA (≈ 153°) and a low WSA (≈ 3°) for a 10 μL droplet (Fig. 4B, C), confirming a typical superhydrophobic state (Supporting Information, Movie S2). In addition, the ZEC-HSW exhibited a markedly reduced interfacial adhesion force ($F_a = 0.04 \times 10^{-3}$ mN) compared to the glass ($F_a = 0.24 \times 10^{-3}$ mN), highlighting the critical role of surface architecture in minimizing liquid–solid adhesion (Figs. 4D). High-speed imaging further demonstrated the dynamic liquid-repellent behavior of the ZEC-HSW (Fig. 4E). A 2 mL water droplet dropped from a height of 8 cm spread rapidly on the ZEC-HSW surface, forming a transient, pancake-like disc. Immediately after reaching maximum expansion, the droplet retracted, coalesced, and rebounded vigorously. In stark contrast, an identical droplet remained pinned on the glass surface after drop, exhibiting only dampened oscillations without rebound, highlighting the role of the micro/nanostructure in reducing adhesion (Supporting Information, Movie S3). This pronounced rebound behavior confirms the stable anti-wetting performance of the ZEC-HSW. The practical self-cleaning capability of the ZEC-HSW was verified via contaminant removal experiments (Fig. 4F). After simple water rinsing, polluted surfaces regained full optical clarity, demonstrating effective rain-assisted cleaning (Supporting Information, Movie S4). This property is essential for maintaining long-term optical performance and stable hydrovoltaic energy harvesting. The ZEC-HSW exhibited robust mechanical durability, with the superhydrophobic surface retaining its performance after 10,000 mechanical friction cycles(Supporting Information, Fig. S10 D, Movie S5). The superhydrophobic behavior is particularly important for the long-term outdoor operation of hydrogel smart windows. For conventional hydrogel-based optical devices, residual water droplets and surface contaminants may scatter incident light and reduce visible transparency. In contrast, the microstructured surface of ZEC-HSW allows water droplets to roll off easily, removing dust and contaminants from the surface. This self-cleaning capability helps preserve the transparent state of the hydrogel window during outdoor exposure and reduces optical degradation caused by environmental contamination. Therefore, the microstructure is not merely used to introduce wettability control, but also acts as a protective surface design for maintaining the optical performance of the smart window.

2.5. Integrated building thermal management and Hydrovoltaic power generation using the ZEC-HSW

The hydrogel layer dynamically modulates light, reducing solar heat gain and indoor temperature for building thermal management. This capability was evaluated using a solar simulator and a thermally insulated model building (Fig. 5A; Fig. S8). Under identical irradiation, the ZEC-HSW model reached only 40 °C after 180 min, versus 47.5 °C for a conventional glass window, demonstrating superior temperature regulation (Fig. 5B). Building energy-saving performance was further evaluated using EnergyPlus simulations based on a ten-story office building model (Fig. S9) across representative climate zones in China. The

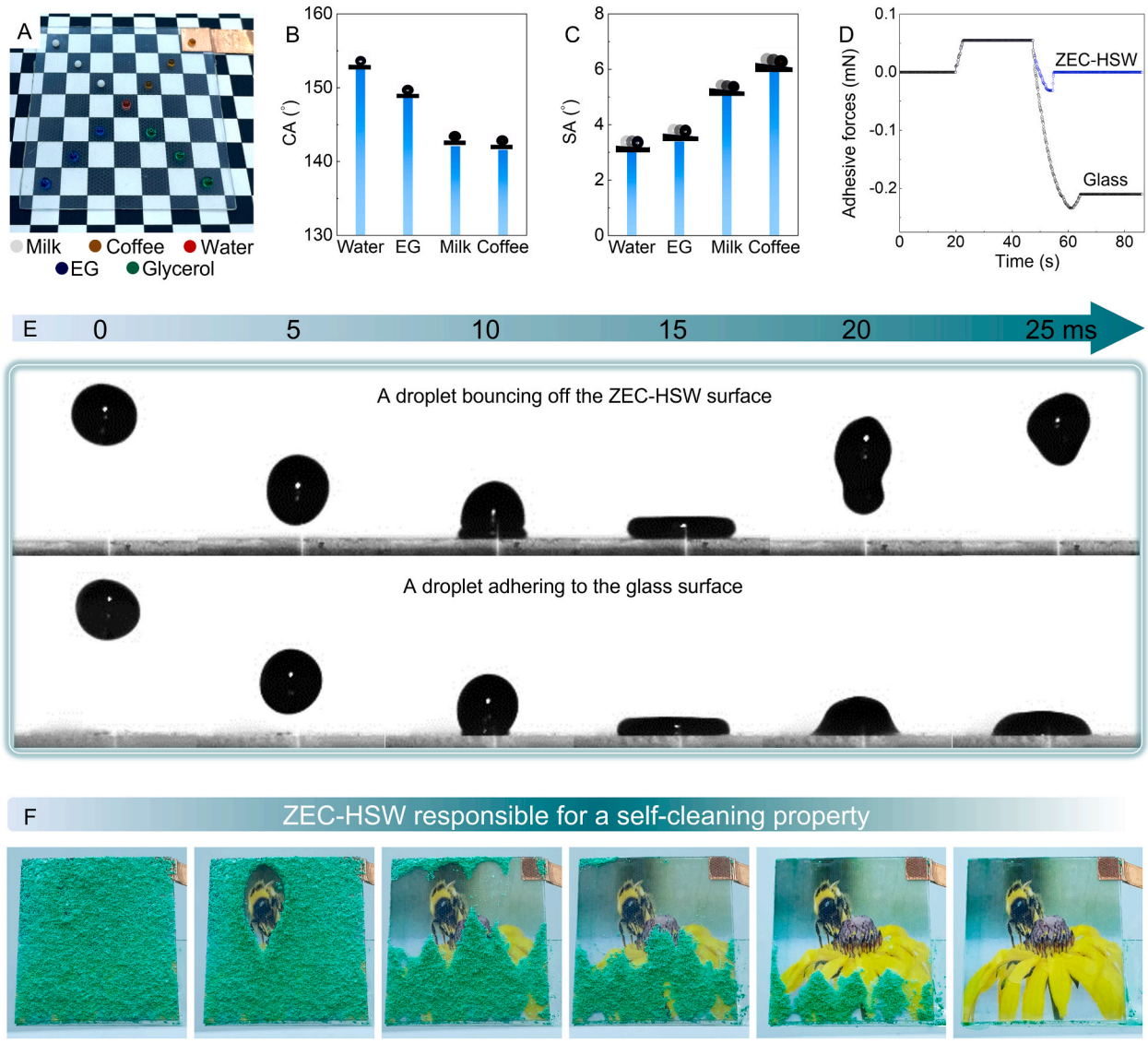

Fig. 4. Superhydrophobicity and self-cleaning performance of the ZEC-HSW surface. (A) Excellent liquid repellency against various inorganic and organic droplets. (B, C) Results of quantitative measurements of contact angles and sliding angles for different liquids (~10 μL). (D) Comparison of interfacial adhesive forces on glass and the ZEC-HSW surface, demonstrating ultralow adhesion on the latter. (E) High-speed imaging sequences comparing droplet impact dynamics on the ZEC-HSW surface (upper) and the glass surface (lower), showing vigorous pancake bouncing versus strong adhesion. (F) Self-cleaning demonstration: surface contaminants are efficiently removed by rolling water droplets, restoring optical clarity.

detailed optical parameters used in the simulations are summarized in Table S1. Compared to conventional glass windows, the ZEC-HSW exhibited pronounced cooling energy savings across all simulated climate zones (Fig. 5C). The annual cooling energy savings reached up to 10,203 MJ in regions with high solar irradiance (Fig. 5D). A corresponding carbon emission analysis revealed an average CO_2 reduction of 1756 kg, with a maximum reduction of approximately 2324 kg in Hainan, China, the region with the highest solar radiation (Figs. 5E, F), highlighting the broad applicability of the ZEC-HSW for energy-efficient buildings. The detailed annual energy savings and carbon emission reductions are summarized in Table S2. It should be noted that the building energy simulations are based on an idealized office building model and climate data. In addition, the analysis focuses on cooling energy savings, and future work will extend to diverse building typologies and full-year energy performance. In addition, the hydrovoltaic functionality of the ZEC-HSW was evaluated under continuous water-droplet impact. As a qualitative visualization of the transient electrical response, the rectified droplet-induced output was used to intermittently illuminate an LED array (Fig. 5G, Movie S6). It should be emphasized that this LED demonstration is intended only to visually indicate the occurrence of droplet-induced charge transfer, rather than to represent continuous power delivery or practical device operation. The electrical output originates from coupled interfacial charge transfer and electrostatic induction during repeated droplet contact and separation on the superhydrophobic surface. Additional electrical characterization, including the short-circuit current, transferred cumulative charge, load-dependent voltage/current curves, peak and average power density, are provided in the Supporting Information (Fig. S12–S14). Moreover, the output voltage increased with the tilt angle from 15° to 60°, reaching a maximum value of 37 V at 60° (Fig. 5H). The ZEC-HSW also maintained stable voltage output during continuous droplet impact for 10,000 s (Fig. 5I), indicating its stable droplet-induced electrical response. To further verify the feasibility of long-term outdoor applications, UV-aging, outdoor exposure, and high-humidity stability tests were conducted. The retained optical performance after UV-aging, outdoor exposure, and high-humidity stability tests (Fig. S10A–C; Movie S7 and S8) confirms the environmental durability of the ZEC-HSW for building-integrated smart-window applications. In addition, the anti-

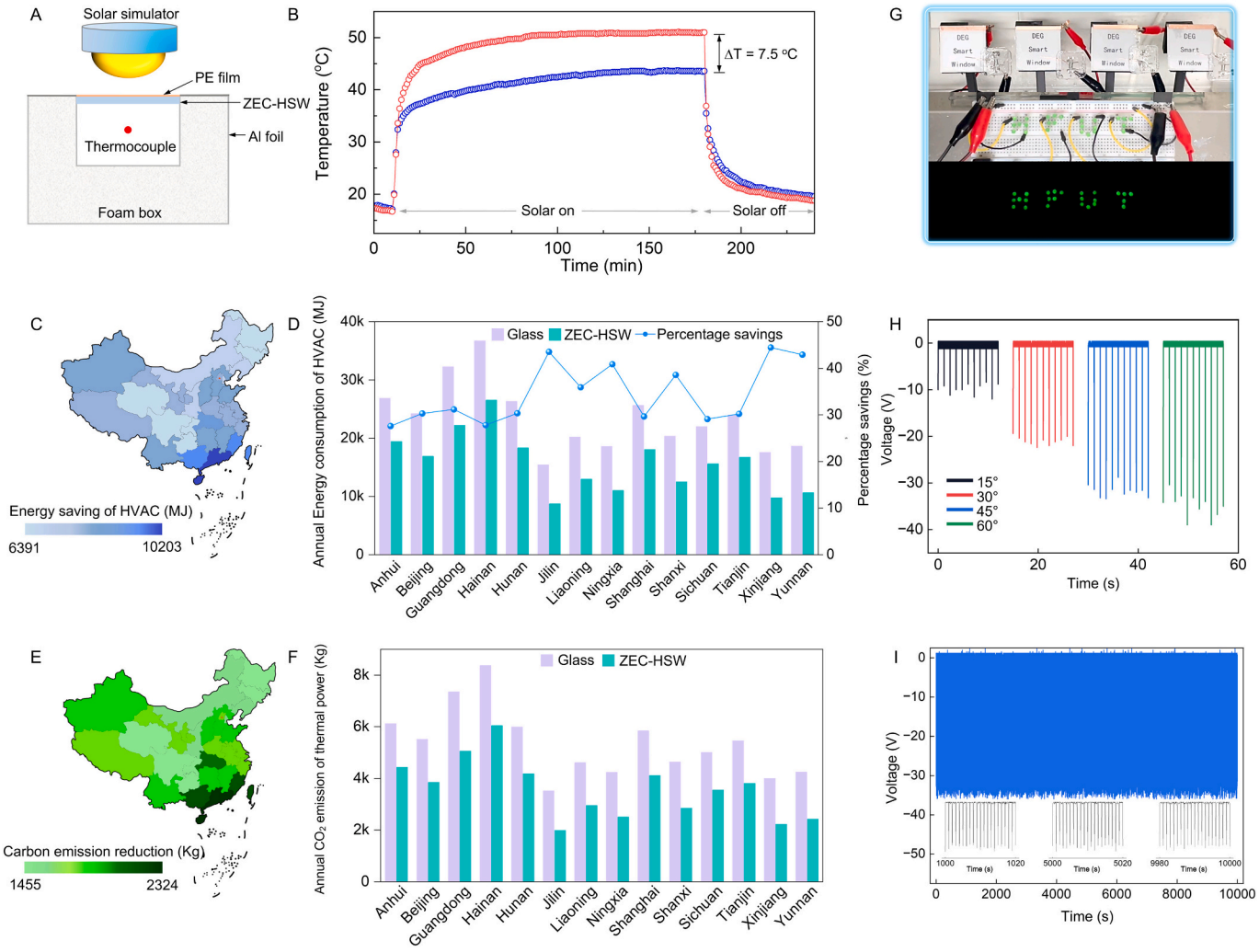

Fig. 5. Thermal regulation and hydrovoltaic energy harvesting applications. (A) Schematic of the experimental setup for indoor temperature monitoring using a model house under solar simulator irradiation. (B) Temperature–time curves for models with glass and ZEC-HSW, demonstrating effective temperature reduction. (C) Simulated annual cooling energy consumption savings of the ZEC-HSW compared to those obtained using conventional glass across different climate zones of China. (D) Comparison of the quantified cooling energy consumption and energy-saving ratio between ZEC-HSW and glass. (E) Simulated annual carbon dioxide emission reductions across different climate zones of China. (F) Quantified CO_2 emissions of ZEC-HSW compared to those of glass. (G) Demonstration of raindrop-driven power generation lighting an LED array. (H) Output voltage as a function of the substrate tilt angle. (I) Long-term voltage output stability under continuous droplet impact for 10,000 s.

contamination performance is demonstrated in Fig. S10E and Movie S9.

3. Conclusion

We propose a high-performance ZEC-HSW fabricated via laser-assisted printing, integrating passive photothermal regulation, superhydrophobic self-cleaning, and hydrovoltaic power generation without external electrical input. Driven by solar and raindrop energy, it achieves a visible transmittance modulation of 61.8% and solar modulation of 46.3%. The bio-inspired superhydrophobic surface (WCA ≈ 153°, WSA ≈ 3°) ensures self-cleaning and long-term stability. It harvests raindrop energy with a ~ 30 V transient output stable over 10,000 s. Building simulations show average cooling energy savings of 34.66% and CO_2 reduction of 1756 kg, with annual cooling energy savings up to 10,203 MJ (~2324 kg CO_2). This work moves beyond single-function smart windows by establishing a microstructure-enabled synergistic design strategy, in which energy saving, self-maintenance, and power generation are structurally coupled within an integrated system. Future work includes large-area fabrication, long-term outdoor durability evaluation, and integration of additional passive energy-management functionalities.

4. Materials and methods

4.1. Materials

The SMP material was prepared using a bisphenol-type epoxy resin precursor and a polyetheramine D230 curing agent (mass ratio 3:1), both purchased from Kunshan Jiulimei Electronic Materials Co., Ltd., China. The ITO glass substrates were sourced from Luoyang Tengchangxukun Biotechnology Co., Ltd., China. NIPAM, HPMC (50 mPa·s), and $NaHSO_3$ were purchased from Aladdin, China. MBA and APS were obtained from Sinopharm Chemical Reagent Co., Ltd., China. The superhydrophobic spray (SF-04172) was purchased from Glaco Mirror Coat Zero, Japan. The double-sided silicone gel tape for the hydrogel reservoir layer was obtained from Nanjing Yinuo Adhesive Products Co., Ltd., China.

4.2. Laser writing of the PTFE template

A regeneratively amplified Ti:sapphire femtosecond laser system (Legend Elite-1 K-HE, Coherent, USA) was used to ablate a hexagonal array pattern (hexagon side length ≈ 500 μm) onto a PTFE film. The typical processing parameters were fixed as follows: laser power of 800 mW, scanning speed of 150 mm s^{-1}, 8 scanning cycles, and a scan area of 4 × 4 cm^2. The resulting template was used for the subsequent soft transfer process.

4.3. Fabrication of the superhydrophobic transparent DEG

Based on the PTFE template, the epoxy resin precursor and curing agent (mass ratio 3:1) were manually mixed for 5 min and then poured into the micro-cavities under a vacuum oven (25 °C, 1 h). Subsequently, a piece of ITO glass (4 × 4 × 0.03 cm^3) with pre-attached copper electrodes was laminated onto the semi-cured layer. The assembly was thermally cured at 65 °C for 4 h. Finally, a commercial superhydrophobic coating (SF-04172, Glaco Mirror Coat Zero, Japan) was sprayed onto the substrate, followed by spin-coating (1000 rpm, 30 s) and thermal treatment (80 °C, 5 min), to obtain the superhydrophobic transparent DEG.

4.4. Preparation of thermoresponsive hydrogel

NIPAM (1.6 g) and HPMC (0.14 g) were dissolved in 7 g of deionized water under magnetic stirring at 70 °C for 1 h until a homogeneous solution was obtained. Subsequently, MBA (5.5 mg), APS (5 mg), and $NaHSO_3$ (3 mg) were added and fully dissolved. The resulting precursor solution was injected into the pre-fabricated sandwich structure, followed by polymerization and crosslinking in a refrigerator at 4 °C for 4 h to obtain the thermoresponsive hydrogel layer.

4.5. SEM sample preparation of hydrogel

For SEM observation of the hydrogel morphology, the hydrogel samples at different thermal states were first frozen at −20 °C until complete solidification and then rapidly transferred to a freeze dryer. The cold-trap temperature was kept below −70 °C, and the vacuum pressure was maintained below 10 Pa. The samples were lyophilized for 48 h to remove water by ice sublimation, yielding freeze-dried porous hydrogel samples for SEM observation.

4.6. Finite-difference time-domain (FDTD) simulations

FDTD simulations analyzed light scattering by the hydrogel using a 2D model with PML boundaries and a TFSF source (0.3–2.5 μm). Pore sizes extracted from SEM images (Fig. S3) ensured realistic microstructure. Frequency-domain monitors recorded scattered fields, and scattering efficiency was calculated as the ratio of integrated scattering cross-section to geometric cross-section. These simulations elucidate the role of microporous structures in regulating light scattering.

4.7. Molecular Dynamics (MD) simulations

Molecular Dynamics (MD) simulations using GROMACS 2023 studied the temperature-driven conformational change of a PNIPAM/HPMC hydrogel. The system contained one NIPAM–MBA–NIPAM chain (31 monomers, 30:1 NIPAM/MBA ratio), six HPMC dimers, and SPC/E water, with OPLS-AA force field and particle mesh Ewald for electrostatics. After equilibration at 293 K, production runs from 293 to 303 K (NPT ensemble) were performed. Radius of gyration and end-to-end distance were analyzed to quantify thermal collapse.

4.8. Energy conversion efficiency calculation

The energy conversion efficiency of the droplet-driven electricity generation process was calculated by comparing the electrical energy output with the gravitational potential energy of a single falling droplet. The input mechanical energy of each droplet was estimated according to:

$$E_{in} = mgh$$

where m is the mass of the water droplet, g is the gravitational acceleration, and h is the falling height. In this work, the volume of each water droplet was approximately 60 μL, corresponding to a mass of 6.0 × 10^{-5} kg. With a falling height of 30 cm, the input energy was calculated to be approximately 176 μJ.

The electrical output energy of a single droplet was estimated from the average output power under the load resistance and the duration of a single electrical pulse:

$$E_{out} = Pt$$

where P is the output power and t is the pulse duration. Under a load resistance of 1 MΩ, the output power was 0.729 mW, and the pulse duration induced by a single droplet was approximately 12.5 ms. Therefore, the output electrical energy was calculated to be approximately 9.1 μJ. The energy conversion efficiency was then determined as:

$$\eta = E_{out}/E_{in} \times 100\%$$

yielding an energy conversion efficiency of approximately 5.2%.

4.9. Characterization

The microstructure of the fabricated array and hydrogel was examined by field emission SEM (JEM-2100F, Japan) and SEM (GeminiSEM 500), respectively. Surface structure dimensions were measured with a laser scanning confocal microscope (OLS5100, Olympus). Phase transition temperatures at 10 °C/min heating/cooling were analyzed by DSC (DSC Q2000). Light intensity around the hydrogel was measured with a visible light intensity meter (FZ-A, Beijing Normal University). Adhesion force was measured with an electronic balance (PX224ZH, OHAUS, USA). Contact and sliding angles (10 μL droplet, 10% RH, 25 °C) were measured by a goniometer (CA100C, INNOO). Optical transmittance/reflectance were measured by UV–Vis-NIR spectrophotometer (3700DUV, Shimadzu) with integrating sphere; absorbance derived from A + R + T = 1. Droplet dynamics (10 μL) were captured at 10,000 fps by a high-speed camera (M210, Revealer, China). Output voltage was recorded by an oscilloscope (Rigol DS1104 plus). Thermal management was tested with a solar simulator (7IS0503A, Saifan Optoelectronics) and a multiplex thermometer (Applent AB4204, China).

CRediT authorship contribution statement

Chao Chen: Writing – original draft, Supervision, Methodology, Conceptualization. **Jianhan Wang:** Writing – original draft, Visualization, Software, Resources, Formal analysis, Data curation. **Peijun Lin:** Data curation. **Kai Shi:** Data curation. **Long Zhang:** Data curation. **Hongwen Zhang:** Writing – review & editing. **Dong Wu:** Writing – review & editing. **Yanlei Hu:** Writing – review & editing, Methodology.

Declaration of competing interest

The authors declare the following financial interests/personal relationships which may be considered as potential competing interests: Chao Chen reports financial support was provided by National Key Research and Development Program of China. If there are other authors, they declare that they have no known competing financial interests or personal relationships that could have appeared to influence the work

reported in this paper.

Acknowledgments

This study was supported by the National Key Research and Development Program of China (2024YFB4610700) and Fundamental Research Funds for the Central Universities (Grant No. JZ2025HGTG0269), and the Natural Science Foundation of Anhui Province (Grant No. JZ2024AKZR0561).

Appendix A. Supplementary data

Supplementary data to this article can be found online at https://doi.org/10.1016/j.cej.2026.179443.

Data availability

Data will be made available on request.

References

[1] X. Li, C. Cao, C. Liu, et al., Self-rolling of vanadium dioxide nanomembranes for enhanced multi-level solar modulation, Nat. Commun. 13 (1) (2022) 7819.
[2] R. Liu, Y. Li, B. Hu, et al., Organic ligand-free scalable dual-band electrochromic smart windows, Adv. Funct. Mater. 35 (1) (2025) 2409914.
[3] Y. Jiang, Y. Wang, D. Kong, et al., A highly visible-transparent thermochromic smart window with broadband infrared modulation for all-season energy savings, Natl. Sci. Rev. 12 (2) (2025) nwae408.
[4] Y. Huang, S. Wu, S. Zhao, et al., A novel liquid flow electrochromic smart window for all-year-round dynamic photothermal regulation, Energy Environ. Sci. 18 (4) (2025) 1824–1834.
[5] B. Chen, Q. Feng, W. Liu, et al., Review on mechanoresponsive smart windows: structures and driving modes, Materials (Basel, Switzerland) 16 (2) (2023) 779.
[6] S.Y. Chun, S. Park, S.I. Lee, et al., Operando Raman and UV-vis spectroscopic investigation of the coloring and bleaching mechanism of self-powered photochromic devices for smart windows, Nano Energy 82 (2021) 105721.
[7] K. Zhang, Y. Shi, L. Wu, et al., Thermo-and pH-responsive starch derivatives for smart window, Carbohydr. Polym. 196 (2018) 209–216.
[8] Y. Ke, J. Chen, G. Lin, et al., Smart windows: electro-, thermo-, mechano-, photochromics, and beyond, Adv. Energy Mater. 9 (39) (2019) 1902066.
[9] M.N. Mustafa, M.A.A.M. Abdah, A. Numan, et al., Smart window technology and its potential for net-zero buildings: a review, Renew. Sust. Energ. Rev. 181 (2023) 113355.
[10] M. Azmat, M.K. Naseem, Hajra, et al., Samarium-doped vanadium dioxide thin films to modulate the thermochromic properties for energy-saving smart windows, ACS Appl. Energy Mater. 7 (9) (2024) 3776–3786.
[11] J. Yang, Q. Li, M. Jing, et al., Lattice stress engineering induced by rare-earth ion in regulating phase transition and thermochromic properties of VO_2 films, Ceram. Int. 49 (21) (2023) 34309–34315.
[12] M. Liu, X. Li, W. Zhang, et al., Three-state thermochromic smart window for building energy-saving, Adv. Sci. 12 (18) (2025) 2416688.
[13] D. Chen, M.H. Chua, Q. He, et al., Multifunctional electrochromic materials and devices recent advances and future potential, Chem. Eng. J. 503 (2025) 157820.
[14] J. Wang, Z. Wang, M. Zhang, et al., Toward next-generation smart windows: an in-depth analysis of dual-band electrochromic materials and devices, Adv. Opt. Mater. 12 (11) (2024) 2302344.
[15] Y. Luo, H. Jin, Y. Lu, et al., Potential gradient-driven fast-switching electrochromic device, ACS Energy Lett. 7 (6) (2022) 1880–1887.
[16] J. Li, X. Lu, Y. Zhang, et al., Highly sensitive mechanoresponsive smart windows driven by shear strain, Adv. Funct. Mater. 31 (32) (2021) 2102350.
[17] M.B. Dharmasiri, T.K. Mudiyanselage, Thermo-responsive poly(N-isopropyl acrylamide) hydrogel with increased response rate, Polym. Bull. 78 (6) (2021) 3183–3198.
[18] N.A. Cortez-Lemus, A. Licea-Claverie, Poly(N-vinylcaprolactam), a comprehensive review on a thermoresponsive polymer becoming popular, Prog. Polym. Sci. 53 (2016) 1–51.
[19] P. Wang, T. Zheng, J. Reitenbach, et al., Solvation dynamics of thermoresponsive polymer films: the influence of salt series in water and mixed water/methanol atmosphere, Adv. Sci. 12 (8) (2025) 2408073.
[20] J. Wang, Y. Lei, H.N. Jaleel, et al., Hydroxypropyl cellulose-based thermochromic hydrogels for smart passive cooling, Adv. Funct. Mater. 36 (6) (2025) 2420946.
[21] X. Du, Z. Xie, H. Zhang, et al., Robust mix-charged polyzwitterionic hydrogels for ultra-efficient atmospheric water harvesting and evaporative cooling, Adv. Mater. 37 (33) (2025) 2505279.
[22] K. Lei, Q. Jiang, D. Gong, et al., Hydrogel smart windows: working mechanisms, recent developments, and perspectives, Small 21 (48) (2025) e10382.
[23] W. Wang, K. Wang, Y. Cheng, et al., Bidirectional temperature-responsive thermochromic hydrogels with adjustable light transmission interval for smart windows, Adv. Funct. Mater. 36 (6) (2026) 2413102.
[24] H. Tu, T. Wang, M. Chen, et al., Isotope-driven hydrogel smart windows for self-adaptive thermoregulation, Nat. Commun. 16 (1) (2025) 6952.
[25] H. Wang, Y. Lu, J. Wang, et al., Hydrated ionic polymer for thermochromic smart windows in buildings, Nat. Commun. 16 (1) (2025) 6509.
[26] Y. Zhou, C. Wan, Y. Yang, et al., Highly stretchable, elastic, and ionic conductive hydrogel for artificial soft electronics, Adv. Funct. Mater. 29 (1) (2019) 1806220.
[27] L. Chen, G. Duan, C. Zhang, et al., 3D printed hydrogel for soft thermo-responsive smart window, Int. J. Extreme Manuf. 4 (2) (2022) 025302.
[28] Y. Zhou, Y. He, S. Qi, et al., Development and evaluation of the energy-saving effect of photothermal cooperative composite hydrogel smart window, Chem. Eng. J. 504 (2025) 158792.
[29] Y. Zhou, S. Wang, J. Peng, et al., Liquid thermo-responsive smart window derived from hydrogel, Joule 4 (11) (2020) 2458–2474.
[30] Z. Na, X. Liang, H. Wang, et al., Broadband modulation, self-driven, and self-cleaning smart photovoltaic windows for high efficiency energy saving buildings, Adv. Funct. Mater. 34 (2) (2024) 2308312.
[31] Y. Shao, J. Zhao, Y. Fan, et al., Shape memory superhydrophobic surface with switchable transition between “Lotus effect” to “rose petal effect”, Chem. Eng. J. 382 (2020) 122989.
[32] W. Weng, M. Tenjimbayashi, W.H. Hu, et al., Evolution of and disparity among biomimetic superhydrophobic surfaces with gecko, petal, and lotus effect, Small 18 (18) (2022) 2200349.
[33] J. Yong, Q. Yang, X. Hou, et al., Nature-inspired superwettability achieved by femtosecond lasers, Ultrafast Sci. 2022 (2022) 9895418.
[34] C. Nakamura, K. Manabe, M. Tenjimbayashi, et al., Heat-shielding and self-cleaning smart windows: near-infrared reflective photonic crystals with self-healing omniphobicity via layer-by-layer self-assembly, ACS Appl. Mater. Interfaces 10 (26) (2018) 22731–22738.
[35] C. Jiang, X. Li, Y. Ying, et al., A multifunctional TENG yarn integrated into agrotextile for building intelligent agriculture, Nano Energy 74 (2020) 104863.
[36] X. Zhang, H. Wang, Y. Miao, et al., Triboelectric nanogenerators for civil infrastructure towards sustainability and intelligence, Nano Energy 148 (2026) 111680.
[37] Z. Li, D. Yang, Z. Zhang, et al., A droplet-based electricity generator for large-scale raindrop energy harvesting, Nano Energy 100 (2022) 107443.
[38] Z. Ma, J. Ai, Y. Shi, et al., A superhydrophobic droplet-based magnetoelectric hybrid system to generate electricity and collect water simultaneously, Adv. Mater. 32 (50) (2020) 2006839.
[39] L. Yang, J. Yu, Y. Guo, et al., An electrode-grounded droplet-based electricity generator (EG-DEG) for liquid motion monitoring, Adv. Funct. Mater. 33 (36) (2023) 2302147.
[40] X. Wei, Z. Zhao, C. Zhang, et al., All-weather droplet-based triboelectric nanogenerator for wave energy harvesting, ACS Nano 15 (8) (2021) 13200–13208.
[41] G. Lee, H. Kang, J. Yun, et al., Integrated triboelectric nanogenerator and radiative cooler for all-weather transparent glass surfaces, Nat. Commun. 15 (1) (2024) 6537.
[42] Q. Zhang, Y. Li, H. Cai, et al., A single-droplet electricity generator achieves an ultrahigh output over 100 V without pre-charging, Adv. Mater. 33 (51) (2021) 2105761.
[43] H. Zhang, K. Yin, L. Wang, et al., A robust droplet triboelectric nanogenerator with self-cleaning ability achieved by femtosecond laser, ACS Appl. Mater. Interfaces 15 (25) (2023) 30902–30912.
[44] N. Zhang, H. Gu, K. Lu, et al., A universal single electrode droplet-based electricity generator (SE-DEG) for water kinetic energy harvesting, Nano Energy 82 (2021) 105735.
[45] Y. Liang S, Y.F. Liu, S.Y. Wang, et al., High-resolution patterning of 2D perovskite films through femtosecond laser direct writing, Adv. Funct. Mater. 32 (38) (2022) 0224957.
[46] H. Liu, N. Wei, M. Li, et al., Polymerization-confined crystallization enables multicolor perovskite nanocomposites via femtosecond laser direct writing, Adv. Funct. Mater. 36 (12) (2026) e15411.
[47] K. Wang, S. Liu, J. Yu, et al., Hofmeister effect-enhanced, nanoparticle-shielded, thermally stable hydrogels for anti-UV, fast-response, and all-day-modulated smart windows, Adv. Mater. 37 (14) (2025) 2418372.
[48] K. Sun, Y. Xie, Q. Lai, et al., Self-adaptive radiative cooling smart windows with spectral band complementary regulation, Energy Convers. Manag. 348 (2026) 120721.
[49] Q. Wang, S. Cao, Q. Meng, et al., Robust and stable dual-band electrochromic smart window with multicolor tunability, Mater. Horiz. 10 (3) (2023) 960–966.
[50] A. Eklund, H. Zhang, H. Zeng, et al., Fast switching of bright whiteness in channeled hydrogel networks, Adv. Funct. Mater. 30 (28) (2020) 2000754.
[51] S. Cho, T.S. Shim, J.H. Kim, et al., Selective coloration of melanin nanospheres through resonant Mie scattering, Adv. Mater. 29 (22) (2017) 1700256.
[52] S. Wu, M. Hua, Y. Alsaid, et al., Poly (vinyl alcohol) hydrogels with broad-range tunable mechanical properties via the Hofmeister effect, Adv. Mater. 33 (11) (2021) 2007829.
[53] K. Wang, G. Chen, S. Weng, et al., Thermo-responsive poly (N-isopropylacrylamide)/hydroxypropylmethyl cellulose hydrogel with high luminous transmittance and solar modulation for smart windows, ACS Appl. Mater. Interfaces 15 (3) (2023) 4385–4397.